VIP Electrocatalysis Very Important Paper

Deutsche Ausgabe: DOI: 10.1002/ange.201510495
Internationale Ausgabe: DOI: 10.1002/anie.201510495

N,P-Codoped Carbon Networks as Efficient Metal-free Bifunctional Catalysts for Oxygen Reduction and Hydrogen Evolution Reactions

*Jintao Zhang, Liangti Qu, Gaoquan Shi, Jiangyong Liu, Jianfeng Chen, and Liming Dai**

Abstract: *The high cost and scarcity of noble metal catalysts, such as Pt, have hindered the hydrogen production from electrochemical water splitting, the oxygen reduction in fuel cells and batteries. Herein, we developed a simple template-free approach to three-dimensional porous carbon networks codoped with nitrogen and phosphorus by pyrolysis of a supermolecular aggregate of self-assembled melamine, phytic acid, and graphene oxide (MPSA/GO). The pyrolyzed MPSA/GO acted as the first metal-free bifunctional catalyst with high activities for both oxygen reduction and hydrogen evolution. Zn–air batteries with the pyrolyzed MPSA/GO air electrode showed a high peak power density (310 $W g^{-1}$) and an excellent durability. Thus, the pyrolyzed MPSA/GO is a promising bifunctional catalyst for renewable energy technologies, particularly regenerative fuel cells.*

Precious metals (e.g., platinum), are commonly used to lower the activation energy barriers for various sluggish electrochemical reactions, such as oxygen reduction reaction (ORR), oxygen evolution reaction (OER), and hydrogen evolution reaction (HER), which are critical to renewable energy technologies.[1] However, their high cost and scarcity have precluded the commercialization of the renewable energy technologies. In order to reduce/replace noble metal (e.g. Pt)-based catalysts, nonprecious metal catalysts (NPMCs) and metal-free heteroatom (e.g., nitrogen)-doped carbons have been developed as efficient catalysts for ORR in fuel cells and bifunctional catalysts for ORR and OER in metal–air batteries.[2] Apart from ORR and OER, the photo/electrocatalytic water splitting to produce hydrogen gas as fuel for fuel cells plays an important role in generating clean energy from sunlight and water.[3] Among NPMCs for HER, metal (oxy)sulfides (e.g., MoS_2) and their derivatives have been widely studied.[4] Carbons are often used as supports for these poorly-conducting catalysts to provide good electron transfer, leading to synergic effects to enhance the HER performance.[5] It is important to understand the intrinsic roles of carbons in these carbon-supported metal-based ORR or HER catalysts and their carbon-based metal-free counterparts.[1a,b,6] Insights thus obtained could be used to guide the development of new carbon-based electrocatalysts,[7] for example as ORR–OER bifunctional catalysts for metal–air batteries[1c] and ORR–HER bifunctional catalysts for regenerative fuel cells.[8]

Although it is still highly challenging to develop carbon-based metal-free bifunctional catalysts, we have recently reported that 3D N,P-codoped mesoporous nanocarbon foams can act as efficient ORR–OER bifunctional catalysts.[1c] Our calculations revealed that the N,P codoping and the graphene edge effect are crucial for the bifunctional electrocatalytic activities. As far as we are aware, however, no carbon-based ORR–HER bifunctional catalyst has been reported, though it is practically important to regenerative fuel cells and other renewable energy technologies.[8] In this work, we have developed a metal-free ORR–HER bifunctional catalyst based on 3D porous graphitic carbons codoped with nitrogen and phosphorus prepared by self-assembling melamine and phytic acid into melamine–phytic acid supermolecular aggregate (MPSA) in the presence of graphene oxide (MPSA/GO), followed by pyrolysis. The obtained catalysts exhibit high catalytic activities towards both HER with a low overpotential and ORR via a four-electron pathway. When the pyrolyzed MPSA/GO was used as the air electrode in a Zn–air battery operated in ambient air, a high peak power density and an excellent durability were achieved. While the low-cost and efficient metal-free carbon-based ORR and HER bifunctional electrocatalysts could advance regenerative fuel cells and water splitting systems to the marketplace, the newly developed simple and scalable methodology should open avenues for low-cost, large-scale production of high-performance carbon-based bifunctional catalysts for renewable energy technologies and beyond.

As shown in Scheme 1, melamine–phytic acid supermolecular aggregate (MPSA) was formed via a simple cooperative assembly of melamine and phytic acid in water at room temperature (Figure S1A in the Supporting Information).[1c] Graphene oxide (GO) with epoxy and hydroxy functional groups on both sides of its surface was used as the pillar

[*] Dr. J. Zhang, J. Liu, Prof. L. Dai
Center of Advanced Science and Engineering for Carbon (Case4-carbon), Department of Macromolecular Science and Engineering, Case Western Reserve University
10900 Euclid Avenue, Cleveland, OH 44106 (USA)
E-mail: liming.dai@case.edu
Prof. L. Qu
Key Laboratory of Cluster Science, Ministry of Education, School of Chemistry, Beijing Institute of Technology, Beijing 100081 (China)
Prof. G. Shi
Department of Chemistry, Tsinghua University
Beijing 100084 (China)
J. Liu, Prof. J. Chen, Prof. L. Dai
State Key Laboratory of Organic-Inorganic Composites, BUCT-CWRU International Joint Laboratory, College of Energy, Beijing University of Chemical Technology, Beijing 100084 (China)
Dr. J. Zhang
Present address: Key Laboratory of Colloid and Interface Chemistry, Ministry of Education, School of Chemistry and Chemical Engineering, Shandong University, Jinan 250100 (China)

Supporting information for this article is available on the WWW under http://dx.doi.org/10.1002/anie.201510495.

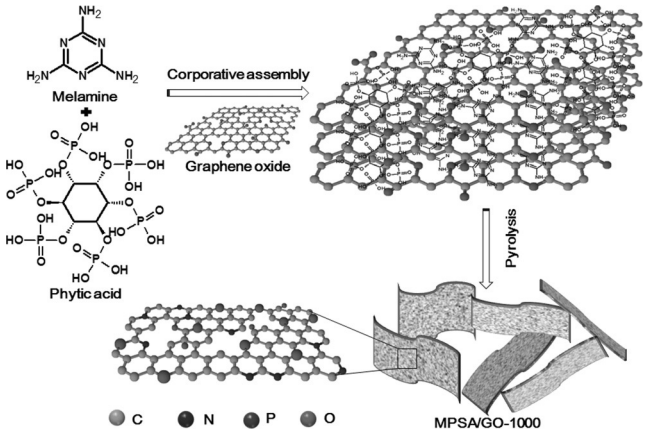

Scheme 1. Preparation process of MPSA/GO-1000 via cooperative assembly and pyrolysis.

connectors to produce MPSA/GO (Figure S1B). Figure S1C reproduces a typical SEM image of the white precipitation shown in Figure S1A, which reveals that the MPSA nanosheets are interconnected with each other to form a foam-like structure. In the presence of GO, nanosheets with relatively large sizes were observed in the SEM image of MPSA/GO (Figure S1D). Subsequent pyrolysis of MPSA/GO led to the formation of 3D graphitic carbon networks at the elevated temperature (e.g., 550–1000 °C). During the pyrolysis process, the nitrogen- and phosphorous-containing functional groups in the melamine and phytic acid precursors, respectively, led to simultaneous codoping of N and P into the final porous graphitic carbons (Figure S2).

Fourier-transform infrared (FTIR) spectroscopy (Figure S3) reveals that the band at 808 cm^{-1} attributable to the triazine ring vibration of melamine shifts to a lower wavenumber (778 cm^{-1}) in MPSA and MPSA/GO due to deformation of the aromatic ring and protonation of the triazine rings in the self-assembled aggregate (cf. Scheme 1). The other broad bands at 960 and 1135 cm^{-1} are assigned to PO_4^{3-} groups, which shift to higher wave numbers (1059, 1185 cm^{-1}), indicating the formation of hydrogen bonding between melamine and phytic acid.[9] Thus, self-assembly of the protonated melamine with phytic acid through hydrogen bonding could lead to the formation of two-dimensional (2D) sheets, which, in turn, were converted into a 3D interconnected network of MPSA via the interlayer π–π stacking (Scheme 1, Figure S1C). Subsequent pyrolysis further converted the MPSA architecture into a 3D carbon network (MPSA-T). The above structure changes were also evidenced by X-ray diffraction (XRD) measurements. As shown in Figure S4A and B, the newly appeared peak at 6.8° for MPSA indicates, most probably, the formation of a 3D layered assembly from the 2D melamine–phytic acid self-assembled nanosheets (Scheme 1) with a large interlayer distance due to the deformation of aromatic rings and/or side groups associated with both the melamine and phytic acid constituents, as indicated by FTIR (see above). The corresponding XRD pattern for MPSA/GO (Figure S4C) shows a significant intensity reduction of the peak at 6.8°, which is accompanied by the appearance of several weak, but noticeable, peaks ($2\theta = 20$–$26°$) with a concomitant narrowing of those high-angle bands characteristic of MPSA. These XRD results indicate that the presence of GO reduced the structure deformation for MPSA and promoted a larger, more ordered 3D layered assembly with a smaller interlayer distance, presumably due to the formation of an interdigitated layer-by-layer assembly with alternating MPSA and GO layers (Scheme 1). The XRD pattern (Figure S4D and E) and Raman spectra (Figure S5) confirm the formation of graphitic carbon during subsequent pyrolysis.[10]

Figure 1 A reproduces the X-ray photoelectron spectroscopy (XPS) survey spectrum for MPSA/GO-1000. The presence of C, N, P and O indicates the formation of the

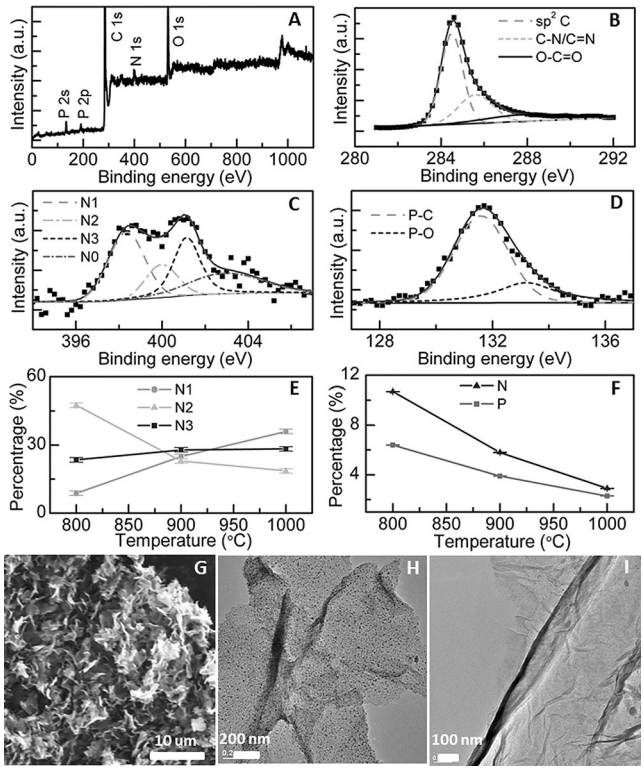

Figure 1. A) An XPS survey spectrum and high-resolution XPS spectra for B) C1s, C) N1s and D) P2p. E) The percentage contents of pyridinic (N1), pyrolic (N2), and quaternary nitrogen (N3) obtained from the XPS measurements for MPSA/GO-1000 and F) the corresponding N and P contents as a function of the pyrolysis temperature. G) SEM and H) TEM images of MPSA-1000 and I) MPSA/GO-1000.

N,P-codoped carbon. In the high-resolution XPS C 1s spectrum (Figure 1 B), the main peak centred at about 284.6 eV is attributable to the graphitic sp^2 carbon whereas the additional component centred at 285.6 eV is assigned to C–N and/or C=N.[11] The low intensity of broad band (287.9 eV, typically O–C=O) suggests that most of the oxygenated groups on GO (Figure S6) have been removed during the thermal treatment.[11] The XPS N 1s spectrum (Figure 1 C) was fitted to pyridinic (398.3 eV), pyrrolic (400.1 eV), graphitic (401.2 eV), and oxidized nitrogen (403.7 eV), respectively.[12] The XPS P_{2p} spectrum (Figure 1 D) shows the P–C bond at about 131.6 eV and P–O

bond at around 133.2 eV.[13] It was further found that the pyridinic and graphitic nitrogen contents increased with increasing the annealing temperature from 800 to 1000 °C whereas the pyrrolic nitrogen content decreased (Figure 2 E),

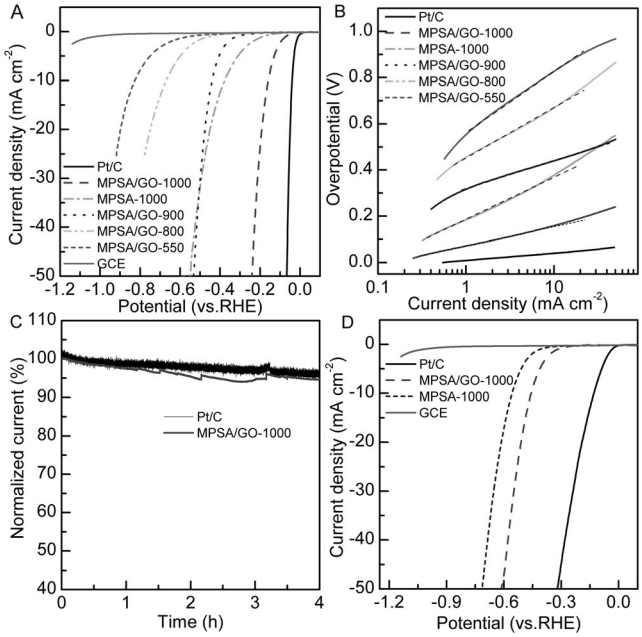

Figure 2. A) Linear scan voltammetry (LSV) curves of various samples for hydrogen evolution in 0.5 M H_2SO_4 and B) the corresponding Tafel curves. C) HER stability tests of the MPSA/GO-1000 and Pt/C electrodes. D) LSV curves of selected samples for hydrogen evolution in 0.1 M KOH.

indicating a thermally induced structure transformation among the different nitrogen species.[14] As shown in Figure 1 F, the thermal treatment could also remove the nitrogen and/or phosphorous heteroatoms through thermal decomposition. Therefore, it is critical to control the pyrolysis temperature to produce MPSA-T and MPSA/GO-T with the desired N and P contents and multidimensional structures.

The SEM image (Figure 1 G) reveals the 3D interconnected network feature of MPSA-1000. The corresponding TEM image in Figure 1 H shows the layered structure of individual carbon sheets with wrinkles. Similar thin carbon sheets are also evident in the TEM image of MPSA/GO-1000 (Figure 1 I). The porous carbon network composed of N,P-codoped graphitic sheets could facilitate the rapid electrolyte and charge transfer for efficient electrocatalysis.[15] The HER catalytic activities of MPSA-T and MPSA/GO-T were measured by linear cycle voltammetry using the commercial Pt/C electrode (C2-20, 20 % platinum on Vulcan XC-72R; E-TEK) as a reference.[5] Figure 2 A shows a temperature-dependent HER activity for MPSA/GO-T samples, with an increased catalytic activity by increasing the pyrolysis temperature (550–1000 °C). The MPSA/GO-1000 exhibited the best HER performance with a low overpotential of 0.06 V (only 60 mV larger than that of Pt/C). At the current density of 30 mA cm^{-2}, the potential of MPSA/GO-1000 is around −0.21 V. These results are much better than those of MPSA-1000 (−0.50 V at 30 mA cm^{-2}) and even recently reported non-noble metal-based HER catalysts (Table S1),[1a,4,16] including the ternary copper molybdenum sulfide (Cu_2MoS_4) (−0.35 V at 12 mA cm^{-2})[17] and RGO–tungsten disulfide composite (−0.30 V at 23 mA cm^{-2}),[18] and comparable to the composites of RGO and copper-centered metal–organic framework as well as MoS_2 (−0.20 V at 30 mA cm^{-2}).[5,19]

Tafel slopes estimated by linear fitting of the polarization curves (Figure 2 B) according to the Tafel equation ($\eta = b \log j + a$, where j is the current density and b is the Tafel slope), are 32, 89, 198, 122, 249, and 250 mV/decade for Pt/C, MPSA/GO-1000, MPSA-1000, MPSA/GO-900, MPSA/GO-800, and MPSA/GO-550, respectively. The MPSA/GO-1000 exhibited the lowest Tafel slope, suggesting, once again, the best reaction kinetics for hydrogen evolution.[1a,7b,20] The HER exchange current densities (j_0) for MPSA/GO-1000 and MPSA-1000 calculated from the Tafel plots by the extrapolation method are 0.16 and 0.12 mA cm^{-2}, respectively, which are comparable and even higher than those of the most reported HER catalysts (Table S1).[1a,4,16] Furthermore, the MPSA/GO-1000 electrode (Figure 2 C) showed an about 95 % current retention after 4 h, similar to that of the Pt/C electrode, clearly indicating the remarkable operation stability. We also tested the HER catalytic activities of MPSA/GO-1000 and MPSA-1000 in various electrolytes (0.1 M KOH in Figure 2 D and K_2SO_4 in Figure S7, respectively). Although Figure 2 D shows higher overpotential values of 0.29 and 0.37 V for MPSA/GO-1000 and MPSA-1000, respectively, than that of the Pt/C catalyst (0.05 V), their remarkable HER catalytic activities are evidenced by the rapid current increase. These results suggest that MPSA/GO-1000 and MPSA-1000 have good catalytic activities for HER over a wide pH range. The superb HER performance observed above for the MPSA/GO-1000 electrode could be attributed to a synergistic effect of N,P codoping. Besides, the 3D porous graphitic network would greatly enhance the electron and electrolyte transports as well as the mechanical and electrochemical stabilities.

To demonstrate the bifunctional catalytic activities, we investigated the ORR performance of the MPSA/GO-T and MPSA-T samples. As shown in Figure 3 A, the ORR catalytic activity of MPSA-1000 is comparable to the Pt/C catalyst with only slightly more negative onset potential and lower diffusion limiting current density. Compared to MPSA-1000, MPSA/GO-1000 showed an even better ORR performance, as evidenced by its more positive onset potential and higher steady-state current density (Figure 3 A).

The LSV curves in Figures 3 B and S8 all show that the expected current increases with increasing scanning rates. The Koutechy–Levich (K–L) plots (Figure 3 C) obtained from the corresponding LSV curves according to the K–L equation [Equation (1) in the Supporting Information] yield the electron transferred number (n) of about 3.5 and kinetic current density (j_k) of 12.9 mA cm^{-2} for the MPSA-1000 electrode (Figure 3 D). As expected, the MPSA/GO-1000 electrode shows a higher electron transferred number (3.7) and kinetic current density (16.9 mA cm^{-2}), which are comparable to those of Pt/C (3.8 and 17.0 mA cm^{-2}), indicating an

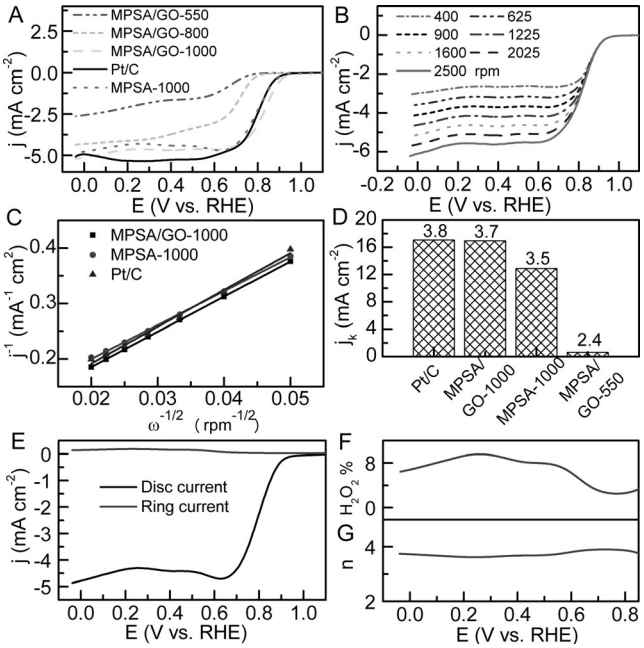

Figure 3. A) LSV curves of MPSA/GO-550, MPSA/GO-800, MPSA/GO-1000, and commercial Pt/C catalyst in O_2-saturated 0.1 M KOH solution. B) LSV curves of MPSA/GO-1000 in O_2-saturated 0.1 M KOH with different rotating speeds. C) The Koutechy–Levich plots for MPSA/GO-1000, MPSA-1000, and Pt/C. D) The kinetic current densities and the electron transferred numbers (on the top of the rectangular bars) for O_2 reduction with various samples at 0.65 V. E) RRDE measurements for MPSA/GO-1000 electrode in O_2-saturated 0.1 M KOH. F) Percentage of peroxide in the total oxygen reduction products. G) The number of electron transfer.

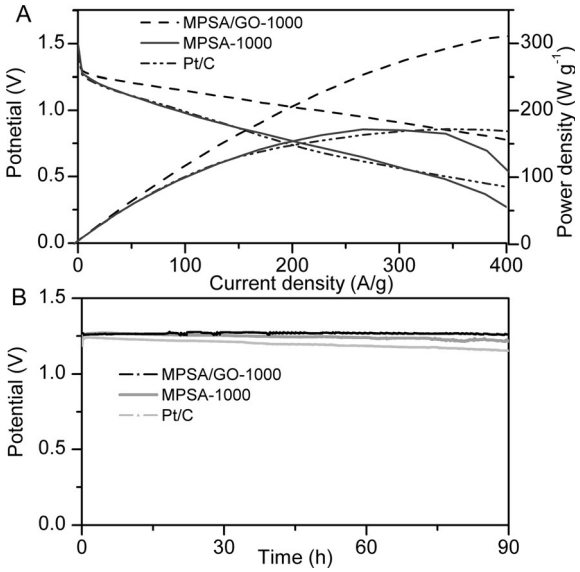

Figure 4. A) Polarization and power density curves, and B) discharge curves of Zn–air batteries using MPSA/GO-1000, MPSA-1000, and Pt/C as the ORR electrocatalyst, respectively.

excellent ORR catalytic activity via a nearly four-electron pathway. Rotating ring-disk electrode (RRDE) measurements also exhibit good ORR performance for the MPSA/GO-1000 electrode with a large disc current and a low percentage of peroxide generation (< 10 %) (Figure 3 E). The electron transferred number calculated from the RRDE data [Equations (3) and (4) in the Supporting Information] is around 3.7. Thus, both the RDE and RRDE measurements suggest an efficient oxygen reduction directly into water via a four-electron pathway. Heteroatom-doping induced charge redistribution has been reported to be responsible for the ORR activity of carbon-based metal catalysts,[2] and codoping with two heteroatoms of electronegativities different from that of carbon has been demonstrated to show a synergistic effect to further enhance the ORR activity.[2d] The observed good stability as well as the high resistance to methanol crossover effect and CO poisoning effect (Figure S9) show the unique features of MPSA/GO-1000 as good ORR catalyst with a high selectivity.

Finally, Zn–air batteries operated in ambient air were fabricated by using MPSA/GO-1000, MPSA-1000, and Pt/C as the ORR electrocatalysts in the air electrode. Figure 4 A exhibits the polarization and power density curves, indicating cell performance comparable to or even better than that of Pt/C electrodes. Specifically, the MPSA/GO-1000 electrode exhibited a higher potential and power density than those of the Pt/C electrode over a large range of current densities (Figures 4 A and S10), suggesting a better rate performance. The peak power density (310 Wg^{-1}) for the Zn–air battery using the MPSA/GO-1000 air electrode is nearly two times that of the battery with the Pt/C air electrode (171 Wg^{-1}) due to the high ORR activity of the MPSA/GO-1000 catalyst and its porous architecture for rapid mass and charge transfer. As shown in Figure 4 B, there is no potential drop for the Zn–air battery using the MPSA/GO-1000 air electrode during the long-time discharging (90 h), which is much better than those of Zn–air batteries using the MPSA-1000 or Pt/C air electrode. The demonstrated good cell performance and durability for Zn–air batteries based on the MPSA/GO-1000 air electrode are consistent with the excellent ORR catalytic activity and stability described above for MPSA/GO-1000. Clearly, therefore, our newly developed metal-free, N,P-codoped 3D carbon networks hold great promise as bifunctional electrocatalysts in various energy devices/systems of practical significance.

In summary, we have developed a simple, low-cost and efficient approach to three-dimensional porous graphitic carbon networks codoped with nitrogen and phosphorus by self-assembling melamine–phytic acid supermolecular aggregate in the presence or absence of GO, followed by pyrolysis. The resultant metal-free carbon catalysts exhibited remarkably high bifunctional electrocatalytic activities with an excellent duribility for both hydrogen evolution and oxygen reduciton reactions. The newly developed MPSA/GO-1000 outperformed most of the metal-based and metal-free carbon-based HER electrocatalysts reported to date while its oxygen reduction performance is comparable to or even better than the state-of-the-art Pt/C electrode. Furthermore, we have fabricated Zn–air batteries by using the as-prepared 3D porous N,P-codoped graphitic carbon networks as the air cathode, leading to a high peak power density (310 Wg^{-1}) and an excellent durability without potential drop over 90 h. This

work represents a major breakthrough in the development of metal-free ORR/HER bifunctional electrocatalysts for renewable energy technologies and beyond.

Acknowledgements

This work was supported by the NSF (CMMI-1400274, CMMI-1266295, DMR 1106160) and the NSFC (21325415, 21174019, 51433005).

Keywords: electrocatalyst · graphitic carbon · hydrogen evolution · oxygen reduction · Zn-air battery

How to cite: *Angew. Chem. Int. Ed.* **2016**, *55*, 2230–2234
Angew. Chem. **2016**, *128*, 2270–2274

[1] a) Y. Zheng, Y. Jiao, Y. Zhu, L. H. Li, Y. Han, Y. Chen, A. Du, M. Jaroniec, S. Z. Qiao, *Nat. Commun.* **2014**, *5*, 3783; b) Y. Jiao, Y. Zheng, M. Jaroniec, S. Z. Qiao, *Chem. Soc. Rev.* **2015**, *44*, 2060–2086; c) J. Zhang, Z. Zhao, Z. Xia, L. Dai, *Nat. Nanotechnol.* **2015**, *10*, 444–452, and references cited therein; d) L. Dai, *Acc. Chem. Res.* **2013**, *46*, 31–42; e) L. Dai, Y. Xue, L. Qu, H.-J. Choi, J.-B. Baek, *Chem. Rev.* **2015**, *115*, 4823–4892; f) J. Zhang, L. Dai, *ACS Catal.* **2015**, *5*, 7244–7253; g) J. Zhang, Z. Xia, L. Dai, *Sci. Adv.* **2015**, *1*, e1500564.

[2] a) K. P. Gong, F. Du, Z. H. Xia, M. Durstock, L. M. Dai, *Science* **2009**, *323*, 760–764; b) L. Qu, Y. Liu, J.-B. Baek, L. Dai, *ACS Nano* **2010**, *4*, 1321–1326; c) S. Wang, E. Iyyamperumal, A. Roy, Y. Xue, D. Yu, L. Dai, *Angew. Chem. Int. Ed.* **2011**, *50*, 11756–11760; *Angew. Chem.* **2011**, *123*, 11960–11964; d) S. Wang, L. Zhang, Z. Xia, A. Roy, D. W. Chang, J. B. Baek, L. Dai, *Angew. Chem. Int. Ed.* **2012**, *51*, 4209–4212; *Angew. Chem.* **2012**, *124*, 4285–4288.

[3] J. Liu, Y. Liu, N. Liu, Y. Han, X. Zhang, H. Huang, Y. Lifshitz, S.-T. Lee, J. Zhong, Z. Kang, *Science* **2015**, *347*, 970–974.

[4] J. Kibsgaard, Z. Chen, B. N. Reinecke, T. F. Jaramillo, *Nat. Mater.* **2012**, *11*, 963–969.

[5] Z.-H. Sheng, L. Shao, J.-J. Chen, W.-J. Bao, F.-B. Wang, X.-H. Xia, *ACS Nano* **2011**, *5*, 4350–4358.

[6] D. S. Su, G. Centi, *J. Energy Chem.* **2013**, *22*, 151–173.

[7] a) H. Jin, J. Wang, D. Su, Z. Wei, Z. Pang, Y. Wang, *J. Am. Chem. Soc.* **2015**, *137*, 2688–2694; b) J. Duan, S. Chen, M. Jaroniec, S. Z. Qiao, *ACS Nano* **2015**, *9*, 931–940.

[8] G. Chen, S. R. Bare, T. E. Mallouk, *J. Electrochem. Soc.* **2002**, *149*, A1092.

[9] J. Xu, G. Wu, Z. Wang, X. Zhang, *Chem. Sci.* **2012**, *3*, 3227–3230.

[10] Z. Lin, G. Waller, Y. Liu, M. Liu, C.-P. Wong, *Adv. Energy Mater.* **2012**, *2*, 884–888.

[11] J. Zhang, J. Jiang, X. S. Zhao, *J. Phys. Chem. C* **2011**, *115*, 6448–6454.

[12] S. Yang, L. Zhi, K. Tang, X. Feng, J. Maier, K. Müllen, *Adv. Funct. Mater.* **2012**, *22*, 3634–3640.

[13] A. M. Puziy, O. I. Poddubnaya, R. P. Socha, J. Gurgul, M. Wisniewski, *Carbon* **2008**, *46*, 2113–2123.

[14] K. Stańczyk, R. Dziembaj, Z. Piwowarska, S. Witkowski, *Carbon* **1995**, *33*, 1383–1392.

[15] W. Ding, Z. Wei, S. Chen, X. Qi, T. Yang, J. Hu, D. Wang, L.-J. Wan, S. F. Alvi, L. Li, *Angew. Chem. Int. Ed.* **2013**, *52*, 11755–11759; *Angew. Chem.* **2013**, *125*, 11971–11975.

[16] a) B. Cao, G. M. Veith, J. C. Neuefeind, R. R. Adzic, P. G. Khalifah, *J. Am. Chem. Soc.* **2013**, *135*, 19186–19192; b) W.-F. Chen, K. Sasaki, C. Ma, A. I. Frenkel, N. Marinkovic, J. T. Muckerman, Y. Zhu, R. R. Adzic, *Angew. Chem. Int. Ed.* **2012**, *51*, 6131–6135; *Angew. Chem.* **2012**, *124*, 6235–6239; c) Q. Liu, J. Tian, W. Cui, P. Jiang, N. Cheng, A. M. Asiri, X. Sun, *Angew. Chem. Int. Ed.* **2014**, *53*, 6710–6714; *Angew. Chem.* **2014**, *126*, 6828–6832; d) X. Zou, X. Huang, A. Goswami, R. Silva, B. R. Sathe, E. Mikmeková, T. Asefa, *Angew. Chem. Int. Ed.* **2014**, *53*, 4372–4376; *Angew. Chem.* **2014**, *126*, 4461–4465.

[17] P. D. Tran, M. Nguyen, S. S. Pramana, A. Bhattacharjee, S. Y. Chiam, J. Fize, M. J. Field, V. Artero, L. H. Wong, J. Loo, J. Barber, *Energy Environ. Sci.* **2012**, *5*, 8912–8916.

[18] J. Yang, D. Voiry, S. J. Ahn, D. Kang, A. Y. Kim, M. Chhowalla, H. S. Shin, *Angew. Chem. Int. Ed.* **2013**, *52*, 13751–13754; *Angew. Chem.* **2013**, *125*, 13996–13999.

[19] M. Jahan, Z. Liu, K. P. Loh, *Adv. Funct. Mater.* **2013**, *23*, 5363–5372.

[20] Y. Zhao, F. Zhao, X. Wang, C. Xu, Z. Zhang, G. Shi, L. Qu, *Angew. Chem. Int. Ed.* **2014**, *53*, 13934–13939; *Angew. Chem.* **2014**, *126*, 14154–14159.

Received: November 15, 2015
Published online: December 28, 2015

